

Counting statistics of chaotic resonances at optical frequencies: theory and experiments

Domenico Lippolis^{1,*}, Li Wang², and Yun-Feng Xiao^{2†}

¹*Faculty of Science, Jiangsu University, Zhenjiang 212013, China and*

²*State Key Laboratory for Mesoscopic Physics and School of Physics,*

Peking University; Collaborative Innovation Center of Quantum Matter, Beijing 100871, China

(Dated: November 15, 2018)

A deformed dielectric microcavity is used as an experimental platform for the analysis of the statistics of chaotic resonances, in the perspective of testing fractal Weyl laws at optical frequencies. In order to surmount the difficulties that arise from reading strongly overlapping spectra, we exploit the mixed nature of the phase space at hand, and only count the high-Q whispering-gallery modes directly. That enables us to draw statistical information on the more lossy chaotic resonances, coupled to the high-Q regular modes via dynamical tunneling.

I. INTRODUCTION

Confinement and manipulation of photons using whispering gallery mode (WGM) microcavities [1–3] have triggered intense research due to their unique features, such as the long photon lifetime and strong field confinement. By breaking the rotational symmetry of the WGM microcavities [4], it was recently found that the deformed microcavities not only gain directionality, highly desirable for microlasers and other photonics applications [5–15], but also serve as dynamical billiards for experimentally testing the systems with a mixed phase space, from which one can study classical and quantum chaos [16, 17]. In particular, prominent phenomena were so far demonstrated experimentally in the optical microcavity system, *e.g.*, dynamical tunneling [10, 18–20], dynamical localization [21, 22], scarring [23–25], turnstile transport [26], and avoided resonance crossings [27].

The study of quasibound states (resonances), of importance to understand the mechanisms of chaotic scattering [28–31], is not so often performed on dielectric microcavities [32]. That is due to both experimental and theoretical challenges. On the experimental side, chaotic resonances are often very lossy, and tend to overlap in the spectrum, making recognition problematic [33]. From a theoretical standpoint, the observations may lend themselves to multiple interpretations [34, 35], due to the *partial* openness of the system, which makes the wave-ray correspondence highly nontrivial [36].

The above issues were specifically addressed in Ref. [37], that deals with the statistics of chaotic resonances in an optical microcavity experiment. In this paper, we present more experiments aimed at estimating the number of *chaotic* resonances from the sole observation of *regular*, mostly WGMs (Fig. 1), together with a thorough analysis, where we test three different models against the experimental data: *i*) a classical prediction, solely based on ray dynamics, *ii*) a known expression [38]

obtained from the truncation of random matrices, and *iii*) a semiclassical correction [39] to *ii*), which depends on the Lyapunov exponent of the chaotic dynamics, and therefore on system-specific properties. Theory, methods, experimental conditions, and statistical analysis are explained in full detail.

The method presented here is intended to set the stage for more general investigations of chaotic scattering phenomena in open systems, beginning with a test at optical frequencies of the fractal Weyl law for the scaling of the number of resonances with the energy [40]. At present, the scaling exponent in this prediction is also believed to depend upon the cutoff chosen for the linewidth [32, 41] of the resonances counted, and thus on the range of decay times of the corresponding chaotic states. With that in mind, an important aspect of the present analysis is that to estimate the typical decay time that the experiments are sensitive to. A comparison of the measured maximum escape rates of the chaotic states with the estimated Ehrenfest time of quantum-to-classical correspondence [42] turns out to provide useful information in that respect.

The paper is organized as follows. Section II contains the theoretical model, with the equations that couple chaotic- to regular modes, obtained with two different but equivalent approaches (Secs. II A and II B, respectively). The key relation between number of chaotic modes and probability of excitation of the regular modes is derived in Sec. II C. The statistics of chaotic modes is treated in Sec. II D with different models, that depend on the timescales involved. In Sec. III A, we place an absorber at the center of the cavity to obtain a full opening. Varying the size of the absorber affects the mean dwell time of the chaotic rays from the cavity. A theoretical study of the statistics of resonances and the number of regular modes excited as a function of the radius of the absorber is presented in Sec. III B, while in Sec. III C we numerically investigate the time scale of transient chaos versus escape to the absorber in the ray dynamics. The experimental apparatus is described in Sec. IV, together with the techniques employed to perform measurements of the transmission spectra, and numerical studies of the prop-

* domenico@ujs.edu.cn

† URL: www.phy.pku.edu.cn/~yfxiao/

agation of both chaotic modes and WGMs inside the cavity. Section V contains the experimental results and their statistical analysis: regular modes are counted in various experimental conditions, and three different models are tested against the data (Secs. VA and VB). As an independent test for our model, we also count statistics of the linewidths of the excited regular modes in Sec. VC. Conclusions and discussion follow suit (Sec. VI).

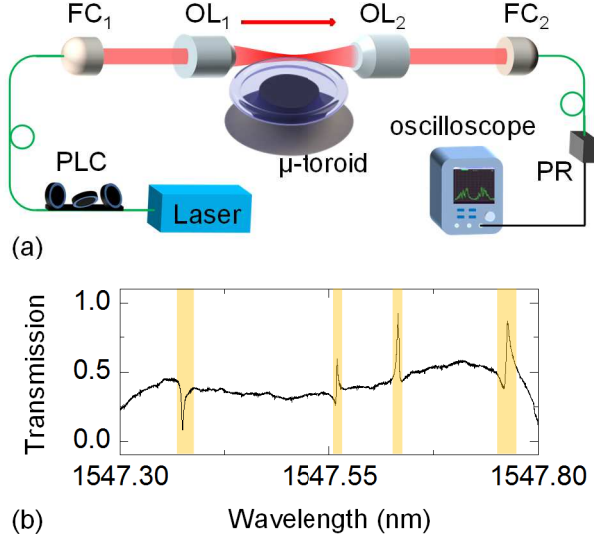


FIG. 1. (color online) (a) Schematic representation of the free-space coupled cavity system: the cavity field is excited by visible or infrared laser light, while the transmitted signal is detected by an oscilloscope. Key: PLC = polarization controller; FC = fiber coupler; OL = optical lens; PR = photon receiver. (b) A typical transmission spectrum with the high- Q regular modes highlighted.

II. THEORETICAL MODEL

Classically, a deformed microcavity allows for both regular and chaotic motion (Fig. 2), which are well separated, so that no trajectory can cross between them. In the quantum picture, however, it is possible for a wave living in one region to leak into the other via dynamical tunneling [43], which introduces a coupling between regular and chaotic resonances.

A. Mode-mode coupling theory

The polarized field [Transverse Electric (TE) or Transverse Magnetic (TM)], excited by the incident beam inside the microcavity, is written as a superposition of one regular (ω) and several (n) chaotic modes [44]:

$$\psi(x, t) = a_\omega(t)c_\omega(x)e^{ik_\omega z - i\omega t} + \sum_n b_n(t)c_n(x)e^{ik_n z - i\omega_n t}. \quad (1)$$

As said, the regular mode is coupled to the chaotic ones via dynamical tunneling, and therefore, one can write a system of response equations [45] under the slowly-varying amplitude assumption [46], and integrate out the spatial part of the modes, to obtain

$$\ddot{b}_n + \omega_n^2 b_n + \gamma_n \dot{b}_n = f_n E_0 - V_n a_\omega, \quad (2a)$$

$$\ddot{a}_\omega + \gamma_\omega \dot{a}_\omega + \omega^2 a_\omega = \sum_n V_n b_n. \quad (2b)$$

Here f_n is the coupling strength of the n -th chaotic mode with the laser beam of amplitude E_0 and frequency ω_0 . V_n (assumed real) is the coupling strength of the n -th chaotic mode with the regular mode, while γ_n and γ_ω are damping rates. Assuming that $\omega_n \approx \omega_0$, one can first set

$$b_n = \text{Re} [b_n e^{-i\omega_0 t}], \quad (3a)$$

$$a_\omega = \text{Re} [a_\omega e^{-i\omega_0 t}], \quad (3b)$$

and then rewrite Eqs. (2) as

$$\dot{b}_n + \gamma_n b_n = f_n E_0 - V_n a_\omega, \quad (4a)$$

$$\dot{a}_\omega + [\gamma_\omega + i(\omega_0 - \omega)] a_\omega = \sum_n V_n b_n. \quad (4b)$$

We are interested in the steady-state solution, obtained by setting $\dot{a}_\omega = \dot{b}_n = 0$. The amplitude a_ω of the envelope of the regular mode is found to be

$$a_\omega = \frac{E_0 \sum_n f_n \frac{V_n}{\gamma_n}}{[\gamma_\omega + i(\omega_0 - \omega)] + \sum_n \frac{V_n^2}{\gamma_n}}. \quad (5)$$

B. An alternative approach

The same equation may be derived in a different way [47, 48]. Consider a Hamiltonian H_0 modelling the closed billiard, whose eigenstates $|a_\omega\rangle$ and $|b_n\rangle$ represent the regular- and chaotic states respectively, uncoupled to one another. The coupling is introduced by the opening, that modifies the Hamiltonian to the non-Hermitian $H = H_0 + V$. Moreover, an incident beam of amplitude E is shone into the cavity. We begin by writing an eigenfunction of H as the superposition

$$|\psi\rangle = a_\omega |a_\omega\rangle + \sum_n b_n |b_n\rangle + E |E\rangle. \quad (6)$$

We have the following coupling properties:

$$\begin{aligned} \langle a_\omega | H | a_\omega \rangle &= \omega - i\gamma_\omega \\ \langle b_n | H | b_n \rangle &= \omega_n - i\gamma_n \\ \langle a_\omega | H | b_n \rangle &= V_n \\ \langle a_\omega | H | E \rangle &= 0 \\ \langle E | H | b_n \rangle &= f_n. \end{aligned} \quad (7)$$

We also assume regular-, chaotic states, and state of the incident beam to be orthogonal to one another [49]. We can now take the Schrödinger equation

$$H|\psi\rangle = \omega_0|\psi\rangle, \quad (8)$$

and sandwich it with

1. $\langle a_\omega |$, to obtain

$$(\omega - i\gamma_\omega) a_\omega + \sum_n b_n V_n = \omega_0 a_\omega \quad (9)$$

2. $\langle b_n |$, and we get

$$b_n = \frac{a_\omega V_n + f_n E}{(\omega_0 - \omega_n) + i\gamma_n}. \quad (10)$$

We now plug Eq. (10) into Eq. (9) to obtain

$$a_\omega = \frac{E \sum_n \frac{f_n V_n}{(\omega_0 - \omega_n) + i\gamma_n}}{(\omega_0 - \omega) + i\gamma_\omega - \sum_n \frac{V_n^2}{(\omega_0 - \omega_n) + i\gamma_n}}. \quad (11)$$

As before, we assume that $\omega_n \simeq \omega_0$ for all chaotic states, which simplifies Eq. (11) to the form

$$a_\omega = - \frac{E \sum_n f_n \frac{V_n}{\gamma_n}}{[\gamma_\omega + i(\omega_0 - \omega)] + \sum_n \frac{V_n^2}{\gamma_n}}. \quad (12)$$

Equation (12) differs from Eq. (5), previously derived, by an overall minus sign, which however does not affect the excitation probability (squared modulus of the amplitude), and by the $\omega_0 - \omega$ term, where the two frequencies are swapped, with respect to Eq. (5).

C. Probability of excitation of a regular mode

Let us now rewrite

$$\sum_n f_n \frac{V_n}{\gamma_n} \simeq n_\gamma \langle \frac{f_n V_n}{\gamma_n} \rangle, \quad (13a)$$

$$\sum_n \frac{V_n^2}{\gamma_n} \simeq n_\gamma \langle \frac{V_n^2}{\gamma_n} \rangle, \quad (13b)$$

where the averages are taken over n_γ chaotic modes of small enough linewidth (γ sets the upper bound) to effectively contribute to the excitation of the regular modes. That way, we can express Eq. (5) as

$$a_\omega = \frac{E_0 n_\gamma \langle \frac{f_n V_n}{\gamma_n} \rangle}{[\gamma_\omega + i(\omega - \omega_0)] + n_\gamma \langle \frac{V_n^2}{\gamma_n} \rangle}. \quad (14)$$

This can be rewritten (setting $\epsilon = \frac{E_0 \langle f_n V_n / \gamma_n \rangle}{\langle V_n^2 / \gamma_n \rangle}$ and $\Gamma = \frac{\gamma_\omega}{\langle V_n^2 / \gamma_n \rangle}$) as

$$a_\omega = \epsilon \frac{n_\gamma}{\left[\Gamma + i \frac{(\omega - \omega_0)}{\langle V_n^2 / \gamma_n \rangle} \right] + n_\gamma}. \quad (15)$$

The excitation probability for the regular mode is therefore

$$|a_\omega|^2 = \epsilon^2 \frac{n_\gamma^2}{(\Gamma + n_\gamma)^2 + \frac{(\omega - \omega_0)^2}{\langle V_n^2 / \gamma_n \rangle^2}}, \quad (16)$$

which becomes, at resonance,

$$|a_\omega|^2 = \epsilon^2 \frac{n_\gamma^2}{(\Gamma + n_\gamma)^2}. \quad (17)$$

D. Statistics of chaotic states

Equation (17) is central to our construction, as it links the number of excited regular modes (proportional to $|a_\omega|^2$), that we measure directly, to the number of chaotic modes n_γ , that we estimate as follows. In principle, we lack information on the typical decay rate/linewidth of the chaotic modes that contribute to the excitation of the regular ones. Specifically, we do not know whether the latter decay within the Ehrenfest time τ_{Ehr} of quantum-to-classical correspondence, or whether they are, on average, significantly longer lived (quasibound). Because of that, we present here three different models, the first entirely classical, the second based on the truncation of random unitary matrices [38], suitable for quasibound states, and the third that combines the previous two [39], and that thus applies to an intermediate timescale.

1. We begin with the classical description, and assume that the motion inside the chaotic part of the phase space is hyperbolic, so that the survival probability takes the form $P(t) \propto e^{-t/\tau_d}$, where τ_d is the mean dwell time of a trajectory in the system. If there are M states in the cavity at $t = 0$, the average number of states that survive in the cavity by time $t^* < \tau_{\text{Ehr}}$ is given by

$$n(t^* < \tau_{\text{Ehr}}) = M e^{-t^*/\tau_d} = M e^{-1/\gamma \tau_d} \quad (18)$$

having set $\gamma = 1/t^*$. In particular, the number of states that survive at the Ehrenfest time is given by

$$n(\tau_{\text{Ehr}}) = M e^{-\tau_{\text{Ehr}}/\tau_d} = M N^{-1/\hat{\mu} \tau_d}, \quad (19)$$

where $\hat{\mu}$ is of the order of the Lyapunov exponent, N is the number of open channels, so that $\tau_d = M/N$, and we took $\tau_{\text{Ehr}} = \hat{\mu}^{-1} \ln N$ (see Appendix A for details).

2. The statistics of the spectrum of a chaotic Hamiltonian is typically determined by means of Random Matrix Theory (RMT) [50]. We now follow this approach in order to estimate the number of long-lived states, starting with an expression for the probability distribution $P(r)$, $r = e^{-\gamma_n/2}$ (γ_n

escape rate of an eigenstate of the open system), obtained from truncated random matrices [38]:

$$\Phi(r) = C \frac{2r}{(1-r^2)^2}, \quad (20)$$

where C is a normalization constant. The number of eigenstates $n_{\gamma, \text{RMT}}$ with escape rate $\gamma_n < \gamma$ is then evaluated from the integral of Eq. (20)

$$n_{\gamma, \text{RMT}} = \int_{r_\gamma}^{\sqrt{1/\tau_d}} \Phi(r) dr \quad (21)$$

with $r_\gamma = e^{-\gamma/2}$, under the assumptions that $\tau_d \gg 1$, and $\lim_{\gamma \rightarrow \infty} n_{\gamma, \text{RMT}} = M - N$, that is the number states that do not decay instantaneously. The final result is

$$n_{\gamma, \text{RMT}} \simeq M \left[1 - \frac{1}{\tau_d} \frac{1}{1 - e^{-\gamma}} \right]. \quad (22)$$

3. If we then want to remove the states that decay within Ehrenfest time from the estimate of n_γ , we just combine (22) and (19), obtaining [39]

$$n_{\gamma, \text{Weyl}} = \frac{M}{N^{1/\mu\tau_d}} \left[1 - \frac{1}{\tau_d(1 - e^{-\gamma})} \right]. \quad (23)$$

The previous expression, which scales as a nonintegral power of the number of states consistently with the fractal Weyl law [39, 41], is therefore a semiclassical correction to the RMT prediction. It depends on the Lyapunov exponent of the chaotic dynamics, and therefore it takes into account system-specific properties.

In what follows, we will validate Eq. (18), Eq. (22), and Eq. (23) respectively against the experimental data.

III. CHAOTIC RAY DYNAMICS AND EXCITATION OF REGULAR MODES

A. Absorber and phase space

In order to achieve the full opening required to test the above predictions, we introduce an absorber in the cavity. In the analysis, the dielectric microcavity (Fig. 2(a), inset) has the deformed circle $\rho(\phi)$ as boundary (see Sec. IV for details), which encloses an absorber of shape $\rho(\phi) - R$. Figure 2 shows the classical phase space, together with the critical line of total internal reflection ($\sin \theta_c$), as well as the line given by the incidence angle θ_a , below which the reflected ray hits the absorber. In what follows we neglect the dependence of θ_a on ϕ by taking the average value, approximately given by the ratio r of the mean radius of the absorber to the cavity's. We assume in this model that the rays that hit the absorber are completely absorbed by it. We will justify the assumption

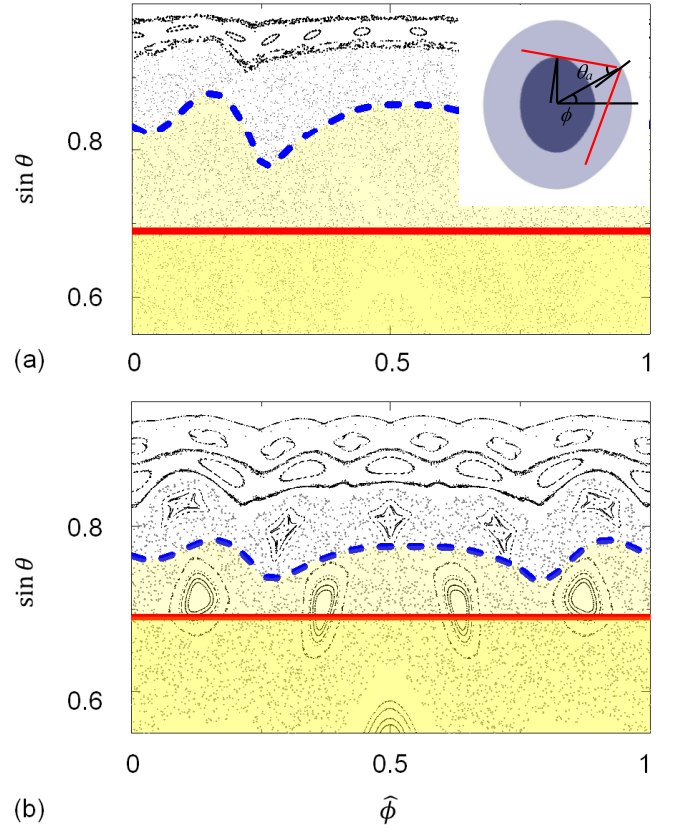


FIG. 2. (color online) (a) (inset) sketch of the deformed microcavity with an inner absorber, characterized by the angle θ_a , and (main) corresponding Poincaré surface of section ($\hat{\phi} \equiv \phi/2\pi$) with deformation factor $\eta = 11.7\%$. The solid red line indicates the angle of total internal reflection, while the dashed curve is given by an absorption angle θ_a such that $r \simeq 0.77$. Different shades of color indicate loss to the absorber (lighter) and by refraction into air (darker). (b) Poincaré section of the microcavity with $\eta = 4.2\%$.

in Sec. IV. We also previously remarked that only a subset of longer-lived chaotic states, out of those available in the whole phase space, effectively contribute to the excitation of the regular modes [Eqs. (13)]. Because of that, we do not count the rays that escape the cavity by refraction into the air with an angle of incidence $\theta \ll \theta_c$, since these are very lossy and they are not expected to contribute to the excitation of the regular modes. Instead, we only take into account the states supported on a strip of the chaotic phase space with momentum above a certain threshold, $\sin \theta > \sin \theta_{\text{th}}$, to be chosen below but close enough to the critical line of total internal reflection. Let us introduce the notation $\xi \equiv \sin \theta_a - \sin \theta_{\text{th}}$ to indicate the strip of the phase space opened by the absorber. The N open channels (rf. Sec. IID) out of the M Planck cells available in the phase space, are produced by the absorber (full opening, N_a) and the refraction out of the cavity (partial opening, N_r), so that the mean dwell

time of a ray is given by

$$\tau_d = \frac{M}{N_a + N_r}, \quad (24)$$

with $N_r = \frac{M}{A} \int_{\sin \theta_a}^{\sin \theta_c} T(\sin \theta) d \sin \theta$, T transmission coefficient according to Fresnel law, and A area of the phase space in exam, while $N_a = M\xi/A$.

The mean dwell time plays a central role in the present study, since the main idea of our experiments resides in counting resonances as a function of the size of the absorber, and therefore in using τ_d as the variable for the predictions (18), (22), and (23).

B. Excitation of the regular modes

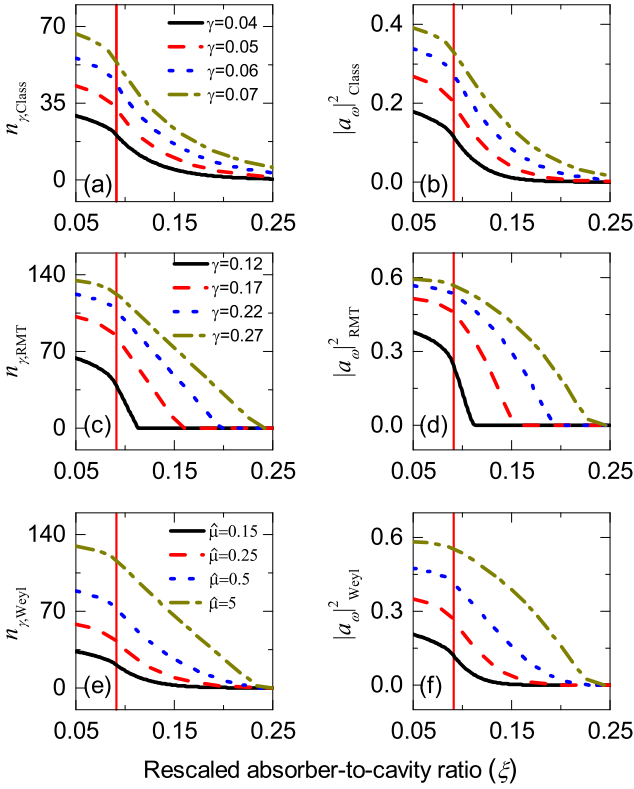


FIG. 3. (color online) (a), (c), (e) Number of chaotic states n_γ vs. the rescaled absorber-to-cavity ratio ξ , obtained by classical, RMT and Weyl law respectively. (b), (d), (f) The corresponding expectations for $|a_\omega|^2$. The red vertical line corresponds to the critical angle, $\sin \theta_c \simeq 0.69$. Here $\sin \theta_{th} = 0.6$.

We proceed by steps and examine the above theories (classical, RMT, semiclassical) for the number of chaotic states n_γ with escape rate less than γ , as a function of the mean dwell time τ_d , or, equivalently, the rescaled absorber-to-cavity ratio ξ . We set $\hat{\xi} = 1/\tau_d = \xi/A + N_r/M$, and rewrite the predictions of section II D in terms of $\hat{\xi}$.

1. The classical model [Eq. (18)] becomes

$$n_{\gamma, \text{Class}} = M e^{-\hat{\xi}/\gamma} \quad (25)$$

in the new notation. Figure 3(a) shows the decay of the number of states as the opening increases in size, and [Fig. 3(b)] the correspondent decay of the probability of excitation of a regular mode: while $n_{\gamma, \text{Class}}$ and $|a_\omega|_{\text{Class}}^2$ [obtained by plugging Eq. (25) into Eq. (17)] decrease slowly for ξ small such that $\theta_a < \theta_c$, that is when the loss is mainly due to refraction into air, both quantities fall off rapidly, and nonlinearly, when the loss is entirely due to the absorber (full opening).

2. The RMT-based prediction, Eq. (22), is also rewritten as a function of $\hat{\xi}$:

$$n_{\gamma, \text{RMT}} = M \left[1 - \frac{\hat{\xi}}{1 - e^{-\gamma}} \right]. \quad (26)$$

Its behavior is illustrated in Fig. 3(c): here $n_{\gamma, \text{RMT}}$ decreases linearly with ξ in the region of total internal reflection, when the loss is entirely due to the absorber. The probability of excitation of the high- Q regular modes $|a_\omega|_{\text{RMT}}^2$ starts to fall off as ξ reaches some critical value, controlled by the parameter γ [Fig. 3(d)]. The other parameter $\tilde{\Gamma} = \frac{\gamma_\omega}{M(V_n^2/\gamma_n)}$ controls the slope of the curve.

3. The semiclassical estimate (23) becomes, as a function of $\hat{\xi}$,

$$n_{\gamma, \text{Weyl}} = \frac{M^{1-\hat{\xi}/\hat{\mu}}}{\hat{\xi}^{\hat{\xi}/\hat{\mu}}} \left[1 - \frac{\hat{\xi}}{1 - e^{-\gamma}} \right]. \quad (27)$$

The rescaled Lyapunov exponent $\hat{\mu}$ of the chaotic region of the phase space is what really characterizes (27), which resembles the linear RMT expression (26) for large enough $\hat{\mu}$, and otherwise becomes visibly nonlinear [Figs. 3(e)] when $\hat{\mu} \ll 1$. This nonlinearity produces a characteristic tail in the probability $|a_\omega|_{\text{Weyl}}^2$ [Fig. 3(f)], similar to that of the classical prediction (18). We therefore interpret it as a classical effect, which is most evident slightly above the onset of chaos.

C. Transient chaos

The survival probability leading to Eqs. (18) and (23) for the classical estimates of the number of decaying states, has an exponential form because it rests on the assumption of a fully chaotic phase space. However, the phase portraits of Fig. 2 suggest the presence of non-hyperbolic ('sticky') regions [51, 52], as well as of partial transport barriers [53, 54] even in the chaotic part of

the phase space, which would make the survival probability decay algebraically, instead of exponentially. We address the issue by performing extensive ray-dynamics simulations of the microcavity-shaped billiard of two different deformation factors, and computing the survival probability in the chaotic region. Here the absorber at the center of the billiard constitutes the sole, full opening. Figure 4 illustrates the results: despite an overall

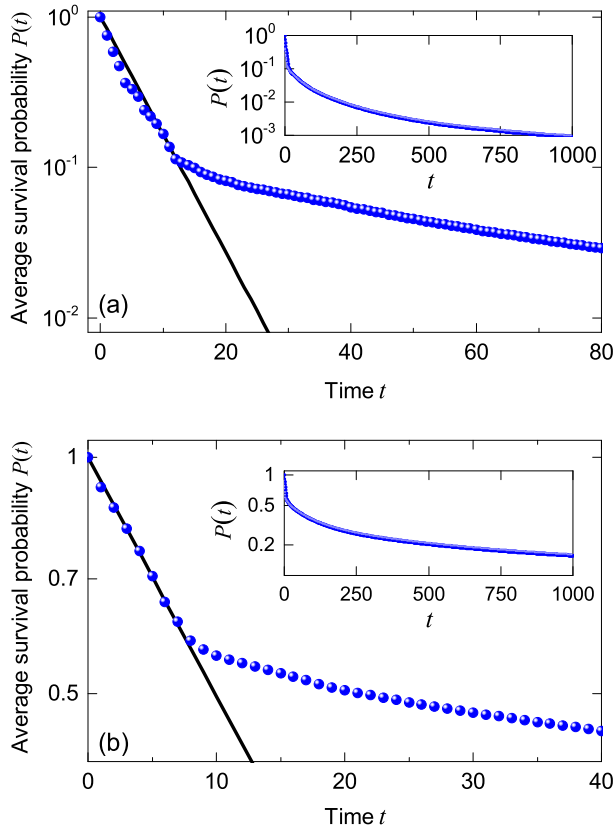


FIG. 4. (color online) Survival probability in the chaotic region (log scale). Points: average survival probability $P(t)$ of a ray in the microcavity vs. t (in units of Poincaré time) at: (a) $\eta = 11.7\%$, $\xi = 0.13$, from 10^6 randomly-started trajectories. Line: $P(t) \propto \exp(-t/\tau_d)$, $\tau_d = 6$; (b) $\eta = 4.2\%$, $\xi = 0.1$, $\tau_d = 14$. Insets: the long-time simulation showing algebraic decay.

power-law decay, a closer look at the short-time dynamics reveals that the decay is initially exponential, behavior known as transient chaos [55]. The applicability of a model involving fully developed chaos would depend on how the Ehrenfest time of quantum-to-classical correspondence compares to the typical transition time τ_{trans} by which the chaotic decay turns algebraic. We estimated $\tau_{\text{trans}} = 6(14)$ units of Poincaré time for a cavity with deformation factor $\eta = 11.7\%(4.2\%)$. We shall estimate the Ehrenfest times of the microcavity of these deformations in Sec. V A, and confirm the validity of the fully chaotic model for the present experiments.

IV. EXPERIMENTAL SETUP AND MEASUREMENT

The experimental apparatus consists of a deformed toroidal microcavity of boundary shape given by the curve

$$\rho(\phi) = \begin{cases} \rho_0(1 + \epsilon \sum_{i=2,3} a_i \cos^i \phi) & \text{for } \cos \phi \geq 0, \\ \rho_0(1 + \epsilon \sum_{i=2,3} b_i \cos^i \phi) & \text{for } \cos \phi < 0, \end{cases} \quad (28)$$

with $\rho_0 = 60 \mu\text{m}$, $a_2 = -0.1329$, $a_3 = 0.0948$, $b_2 = -0.0642$, and $b_3 = -0.0224$. The WGMs in the deformed microcavity have been demonstrated to possess ultrahigh quality factors in excess of 10^8 in the 1550 nm wavelength band and to exhibit highly directional emission towards the 180° far-field direction, which emits tangentially along the cavity boundaries at polar angles $\phi = \pi/2$ and $\phi = 3\pi/2$ [20]. The deformation is controlled by $\eta = (d_{\text{max}} - d_{\text{min}})/d_{\text{max}}$, d_{max} and d_{min} respectively the maximum and minimum diameters of the cavity. The parameter η is related to ϵ through $\eta = \epsilon |a_2 + a_3 + b_2 - b_3|/2$. The microcavity is coupled to a free-space propagating laser beam of wavelength $\lambda \simeq 1550 \text{ nm}$ or 635 nm , as shown in Fig. 1. The microtoroid (refractive index $\simeq 1.44, 1.46$ depending on λ , Fig. 5) has principal/minor diameters of $120/5 \mu\text{m}$, consistently with the two-dimensional model. Thus the ef-

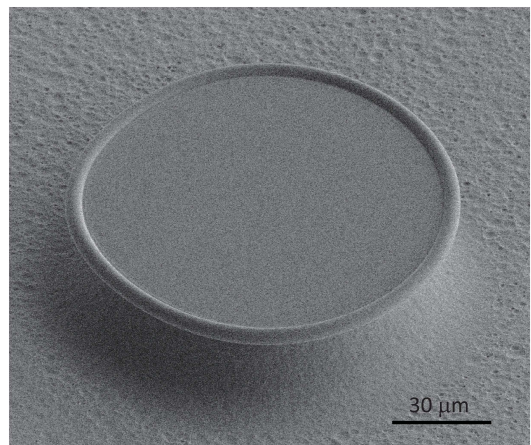


FIG. 5. Image of the microcavity obtained by Scanning Electron Microscopy (SEM).

fective Planck constant $h_{\text{eff}} \sim \lambda/a \sim 10^{-2}$ (a : principal diameter) justifies the semiclassical analysis. The microcavity is fabricated through optical lithography, buffered HF wet etching, XeF_2 gas etching, and CO_2 pulse laser irradiation. The resulting silica microtoroid is supported by a silicon pillar of similar shape, which has a high refractive index ($\simeq 3.48, 3.88$), and it acts as the absorber in the model. After each measurement of the transmission spectrum (Fig. 8), the top diameter of the silicon pillar, connected with the silica disk, is progressively reduced by a new isotropic XeF_2 dry etching process. In this way we control the openness of the microcavity with

the ratio r between the top diameters of pillar and toroid. Finite-element method simulations (Fig. 6) show that the light power decreases to less than 5% of the input value, when propagating by a distance of 20 μm inside the 2- μm -thick silica waveguide bonding with a silicon wafer, as it is reasonable to expect, given the high refractive index of the silicon. Thus the silicon pillar acts

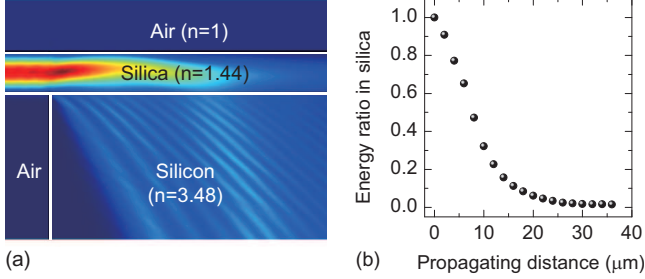


FIG. 6. (color online) (a) Finite-element method simulation of the light propagating inside the 2- μm -thick silica waveguide bonding with a thick silicon layer (color scale in arbitrary units). (b) Fraction of remaining energy in silica vs. the propagating distance.

as a full absorber, consistently with the model presented here. On the other hand, high- Q regular modes living inside the toroidal part, whose circular cross section has diameter of 5 μm , do not leak into the silicon pillar and therefore are not directly affected by the pillar size. Figure 7(b) illustrates the numerical simulation of a regular TE mode, that is confined in the toroidal region. Due to

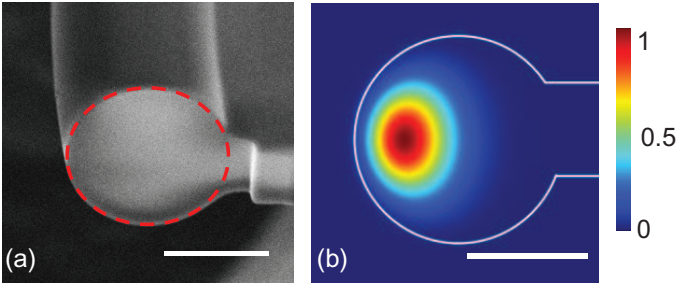


FIG. 7. (a) SEM cross-section image of the microtoroid, taken at an angle of 56° with the horizontal direction. (b) Finite-element method simulation of a fundamental TE mode (color scale in arbitrary units). The white solid curve is the boundary of the cavity. The scale bar is 3 μm in both (a) and (b).

the free-space propagation, the laser beam can only enter the cavity with a relatively large angle of incidence, and therefore it couples with the chaotic cavity modes, which in turn couple with the regular modes via dynamical tunneling, consistently with the model of Sec. II. The dependence of the transmission spectra on the pillar size is shown in Fig. 8. When the pillar approaches the inner edge of the toroid (Figs. 8(a) and 8(e), $r \simeq 0.81$), no high- Q regular modes are observed in the spectrum, since most of the probe laser field in the cavity radiates

into the silicon and cannot tunnel to couple with high- Q regular modes. As we gradually reduce the size of the pillar [Fig. 8(f), $r \simeq 0.77$], increasingly many high- Q modes appear in the spectrum [Fig. 8(b)]. When the absorber-to-cavity ratio r is small enough (Figs. 8(g) and 8(h), $r \lesssim 0.7$), the transmission no longer changes sensibly [Figs. 8(c) and 8(d)], and the number of high- Q modes in the spectrum also stabilizes.

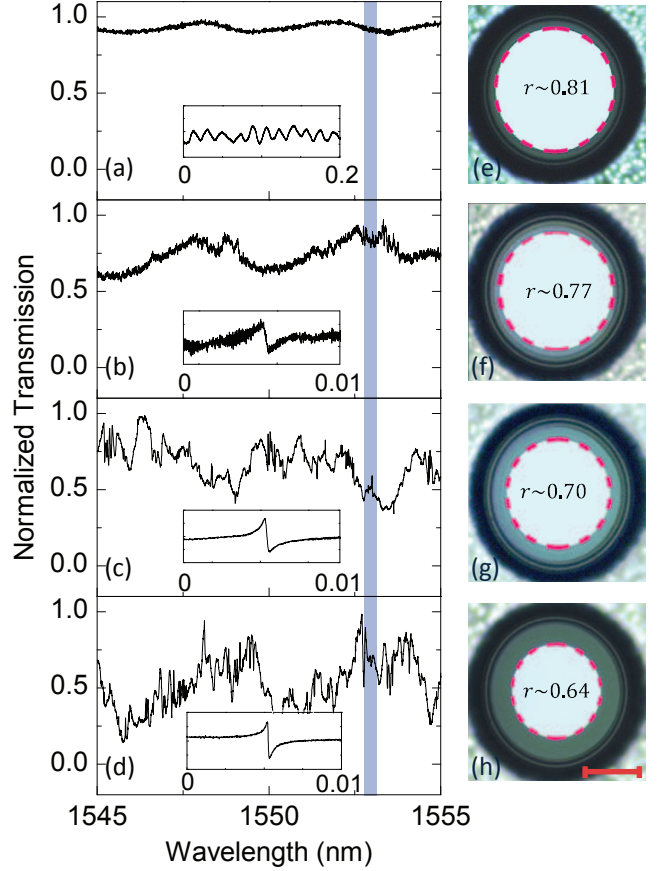


FIG. 8. (color online) Normalized transmission and top-view optical images of the cavity with $r \simeq 0.81$ [(a) and (e)], 0.77 [(b) and (f)], 0.70 [(c) and (g)], 0.64 [(d) and (h)]. Inset of (a) shows background noise. Insets of (b)-(d) show the high- Q modes. Reflection of the silica-to-silicon interface results in a brighter color for the silicon pillar in the optical image (boundary shown by red dashed curves). Scale bar is 50 μm . Adapted from Ref. [37].

V. STATISTICS OF CHAOTIC RESONANCES

As anticipated, we use the transmission spectra to test the theory, by counting the excited high- Q regular modes for different sizes of the silicon pillar. A polarization controller is used to alternatively excite TE- or TM modes, which are collected by the photon receiver, and read from the transmission spectra. We single out and add up the modes with high Q factors ($Q > 10^5$) for both polar-

izations, but since TE- and TM modes are not perfectly orthogonal to each other in the real microcavity, some may be counted twice, which is the main source of uncertainty in our data.

A. Classical model

Once the data are collected, we test all the predictions presented in the theoretical sections, starting with the classical model. Equation (25) is plugged into Eq. (17), and fitted to the data via the parameters $\tilde{\Gamma}$, γ up to an overall multiplicative constant. The total number of chaotic states is estimated theoretically as $M \simeq A/h_{\text{eff}}$ (A area of the phase space we consider). The results are shown in Fig. 9, with details in Table I. The classical pre-

TABLE I. Parameters related to the best-fit of Eq. (25) to the data, and to the experimental conditions. Here γ is expressed in units of T^{-1} , with $T \simeq 3 \cdot 10^{-13}$ s Poincaré time.

$\tilde{\Gamma}$	γ	η	$\lambda(\text{nm})$	M	χ^2
$6 \cdot 10^{-4}$	0.009	4.2%	630	40	4.4
0.003	0.014	4.2%	1550	20	1.7
0.01	0.013	6.0%	630	40	2.6
0.008	0.015	6.0%	1550	20	0.95
0.005	0.017	11.7%	1550	25	0.85

diction appears to fit the data rather well, overall. The statistical test of χ^2 [56] evaluates the average discrepancy between expectations $[n_{\gamma, \text{Class}}(\xi_i)]$ and observations $(n_{\gamma, i})$, divided by the experimental errors σ_i , in d degrees of freedom:

$$\chi^2 = \frac{1}{d} \sum_i \frac{[n_{\gamma, i} - n_{\gamma, \text{Class}}(\xi_i)]^2}{\sigma_i^2}. \quad (29)$$

Here we generally obtain $\chi^2 \approx 1$, indicating that the extent of the match between observations and estimates is in accord with the error variance. However, in order for this model to be accurate, all the chaotic states indirectly detected by the experiment should decay within Ehrenfest time, which seems unlikely, in principle. The minimum decay time of the chaotic modes is determined from the best fits as γ^{-1} , and it can be compared with the Ehrenfest time (we should find $\tau_{\text{Ehr}} > \gamma^{-1}$), with the latter estimated in terms of the laser wavelength, the dimensions of the cavity, the Lyapunov exponent of the classical dynamics, and the size of the absorber (see Appendix C for details). In this regard, the absorber-to-cavity ratio ξ varies within a certain range, thus we estimate upper and lower bounds for τ_{Ehr} in units of the Poincaré time T , as summarized in Table II, for cavities of different deformations, coupled to either visible or infrared light. As we can see, the estimated Ehrenfest time of the rays in the microcavity is always significantly shorter than the minimal escape time γ^{-1} , although of the same order of magnitude. That suggests that the classical model for

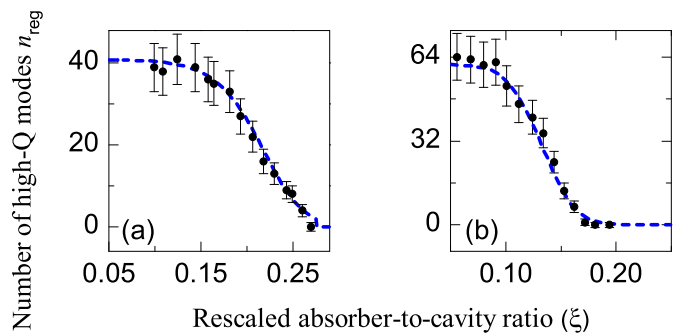


FIG. 9. (color online) Dots: number of high- Q regular modes (n_{ω}) observed in the transmission spectra of the microcavity coupled to infrared light, as a function of rescaled absorber-to-cavity ratio ξ . Blue dashed curve: best fit of the classical prediction (25) [together with Eq. (17)]. Left: $\eta = 11.7\%$; right: $\eta = 6\%$. Here $\sin \theta_c \simeq 0.69$ and $\sin \theta_{\text{th}} = 0.6$.

TABLE II. Lower and upper bounds for the typical Ehrenfest time (in units of Poincaré time) of the chaotic states of microcavities with different deformation factors, coupled to either infrared or visible light, in comparison with the average γ^{-1} coming from the fitting parameters in Table I.

η	$\lambda(\text{nm})$	$\tau_{\text{Ehr}}^{\text{min}}$	$\tau_{\text{Ehr}}^{\text{max}}$	γ^{-1}
4.2, 6%	630	6.5	14.	94
4.2, 6%	1550	15	25	70
11.7%	1550	10	14	59

the statistics of the chaotic states alone does not describe the experiment consistently.

B. RMT- and semiclassical predictions

Next, we validate *i)* the RMT-based prediction (26), and *ii)* the semiclassical expression (27), which we alternatively plug into the probability of excitation of the regular modes, Eq. (17). The results are illustrated in Fig. 10 (details in Tables III and IV), for two microcavities of distinct deformations, probed at visible and infrared wavelengths.

In the RMT-based approach we have two fitting parameters, γ and $\tilde{\Gamma}$. Figure 10 shows overall agreement

TABLE III. Parameters related to the best-fit of Eq. (26) to the data, and to the experimental conditions in Fig. 10. Here γ is expressed in units of T^{-1} , with $T \simeq 3 \cdot 10^{-13}$ s Poincaré time.

$\tilde{\Gamma}$	γ	η	$\lambda(\text{nm})$	M	χ^2
2.1	0.11	4.2%	630	40	14
0.9	0.14	4.2%	1550	20	9.4
4.4	0.12	6.0%	630	40	12
0.6	0.12	6.0%	1550	20	22
0.75	0.15	11.7%	1550	25	3.3

between the experimental data and this theory, which

however fails to capture the tail visible at larger sizes of the absorber. Such discrepancy is consistent over all

the realizations of the system, and it results in a χ^2 that significantly differs from the optimal value of unity.

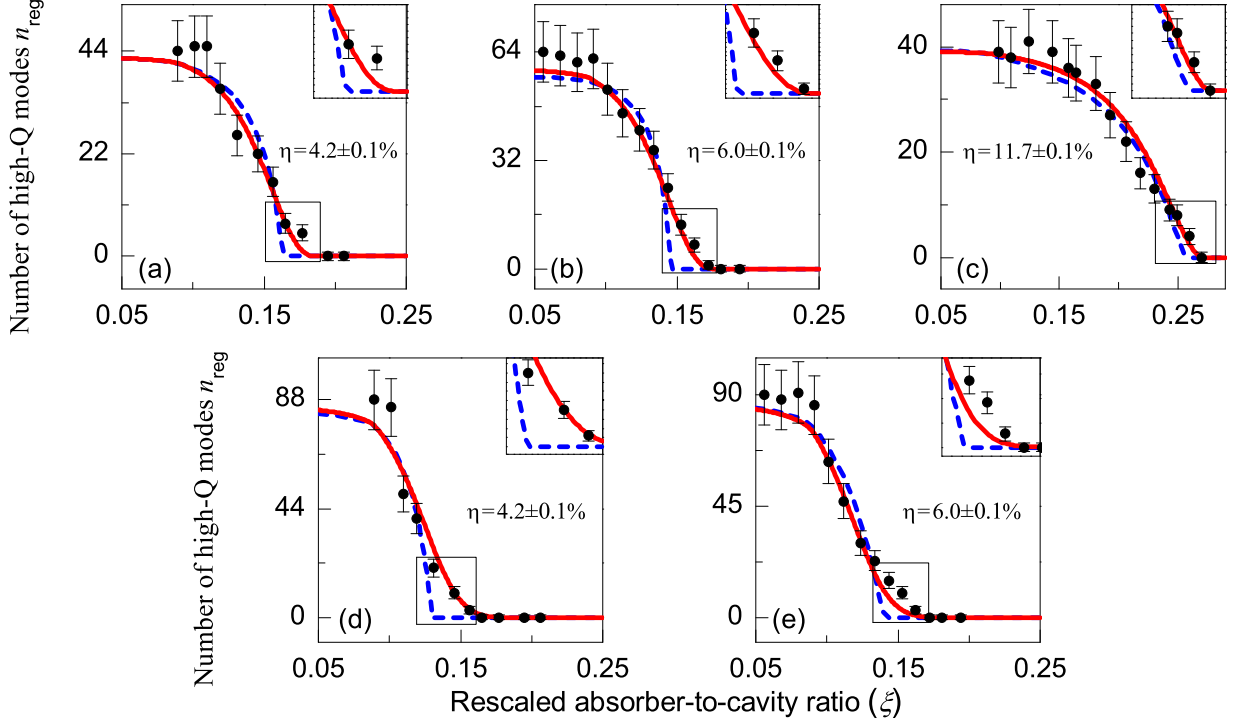


FIG. 10. (color online) Number of high- Q regular modes (n_{reg}) observed in the transmission spectra of the microcavity (dots), as a function of rescaled absorber-to-cavity ratio ξ . Blue dashed- and red solid curves are respectively RMT- and semiclassical prediction best fits. (a), (b), (c): infrared light; (d), (e): visible light. Here $\sin \theta_c \simeq 0.69$ and $\sin \theta_{\text{th}} = 0.6$. Insets: the area where the two curves differ most.

We evaluate the semiclassical correction (27), using the finite time Lyapunov exponent $\hat{\mu}$ evaluated by direct iteration, over a short enough time for the dynamics to be still hyperbolic (cf. Sec. III C). In addition to that we still have the estimated parameter M and the fitted parameters γ and Γ . This expression is found in better agreement with the experimental data ($\chi^2 \approx 1$) than the RMT-based estimate, especially at the smaller deformation, where the two predictions differ the most due to the smaller $\hat{\mu}$ [cf. Fig. 3]. In particular, the semiclassical theory accounts for the tail of the curve, that corresponds to the microcavity having the largest openings and thus with the maximum number of instantaneous decay states, where the semiclassical correction is decisive.

Similarly to the classical model, we check whether the fitted values of the parameter γ make physical sense. It is found that, typically, $\gamma \simeq 0.14$; now recall that $\gamma^{-1} = \tau_{\text{esc}}$ the minimum escape time of the chaotic rays contributing to the excitation of the regular modes, from which $Q = 2\pi\nu\tau_{\text{esc}} \sim 10^3$, on average (ν is the frequency of the laser beam). We find this estimate consistent with the typical order of Q independently obtained from ray-

TABLE IV. Parameters related to the best-fit of Eq. (27) to the data, and to the experimental conditions in Fig. 10. Here γ and μ are expressed in units of T^{-1} , with $T \simeq 3 \cdot 10^{-13}$ s Poincaré time.

Γ	γ	η	$\lambda(\text{nm})$	M	μ	χ^2
0.5	0.16	4.2%	630	40	0.05	2.6
0.27	0.16	4.2%	1550	20	0.05	1.7
0.7	0.16	6.0%	630	40	0.05	2.9
0.4	0.15	6.0%	1550	20	0.05	1.5
0.42	0.17	11.7%	1550	25	0.1	1.5

dynamics simulations (in Fig. 11), which corroborates the result from the analysis. By the same token, one can write the linewidth of a resonance as $\text{Im } \Omega = -\frac{a}{2c}\gamma$, where again a is the cavity radius and c the speed of light inside the silica. We estimate on average $\text{Im } \Omega \simeq -0.1$, which is close to the median value $\text{Im } \Omega \simeq -0.15$ of the distribution of resonances found in the numerical experiment of ref. [32], where a stadium-shaped microcavity of refractive index $n = 1.5$ was considered. At last, but importantly, we compare γ^{-1} with the Ehrenfest time.

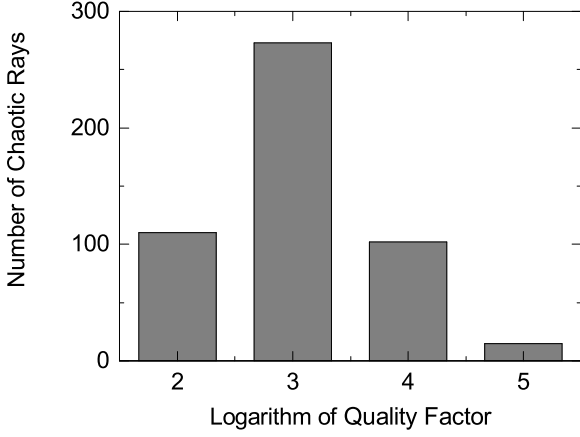


FIG. 11. Statistics of the quality factor for the chaotic rays in the deformed microcavity, from a ray-dynamics simulation.

Equations (26) and (27) are based on the assumption $\tau_{Ehr} < \gamma^{-1}$, the opposite of the classical model's. We find from our fits (Tables III and IV) that $\tau_{Ehr} \approx \gamma^{-1}$ in all the realizations of the experiments, and therefore, the above assumption is not always validated within the uncertainties. We believe at the present stage the semi-classical prediction to be a more accurate model for the statistics of the chaotic states than the entirely classical one. All the same, a number of chaotic states that escape within Ehrenfest time may also contribute to the excitation of the regular modes, for our experiment to capture that intermediate time scale at the border line between classical and purely wave-like modes. One could at that point combine theories using the following expression [57]:

$$n_\gamma = \varepsilon n_{\gamma, \text{Class}} + (1 - \varepsilon) n_{\gamma, \text{Weyl}}, \quad (30)$$

which would, however, add one presently unknown parameter (ε) to the analysis.

C. Statistics of the regular modes and their linewidths

The approximations (13)

$$\begin{aligned} \sum_n f_n \frac{V_n}{\gamma_n} &\simeq n_\gamma \left\langle \frac{f_n V_n}{\gamma_n} \right\rangle, \\ \sum_n \frac{V_n^2}{\gamma_n} &\simeq n_\gamma \left\langle \frac{V_n^2}{\gamma_n} \right\rangle, \end{aligned}$$

leading to Eq. (17) for the probability of excitation of a regular mode, in fact replace distributions with their averages (first moments), and ignore the fluctuations of the quantities involved (couplings and damping rates). In order to understand whether and to what extent the present experiment allows that approximation, we derive

an expression relating the mean linewidth of a regular mode $\gamma_{\text{reg}}^{\text{tot}}$ with the observed number of regular modes n_{reg} , which we then test with the experimental data.

Looking at Eq. (5) for the amplitude of a regular mode, we can regard the term

$$\gamma_\omega^{\text{tot}} = \gamma_\omega + \sum_n \frac{V_n^2}{\gamma_n} \quad (32)$$

as the total (hence measured) linewidth [44], where the first term indicates the intrinsic linewidth of the regular mode, while the second represents the decay into the chaotic modes. That already suggests that $\gamma_{\text{reg}}^{\text{tot}}$ increases with n_γ . If the fluctuations ultimately due to the dependence of these quantities on the frequency ω of the mode can be neglected, say, to a zeroth-order approximation, we should be able to see that trend in the experiment.

Since we do not measure n_γ directly, we express γ_{tot} in terms of n_{reg} , the number of regular modes, which is

$$n_{\text{reg}} = \kappa \frac{n_\gamma^2}{(\Gamma + n_\gamma)^2}, \quad (33)$$

from (17), assuming that n_{reg} is simply proportional to the probability of excitation of one mode, and thus once again dropping the dependence on ω . That way, we replace $\gamma_\omega^{\text{tot}}$ with the average $\gamma_{\text{reg}}^{\text{tot}} = \gamma_{\text{reg}} + n_\gamma \left\langle \frac{V_n^2}{\gamma_n} \right\rangle$, and then write n_γ as a function of the observed quantity n_{reg} , by solving the quadratic equation (33)

$$n_\gamma = \Gamma \frac{n_{\text{reg}} + \sqrt{n_{\text{reg}}^2 - n_{\text{reg}} + \kappa}}{k - n_{\text{reg}}}. \quad (34)$$

Recalling the definition of Γ , we have

$$\gamma_{\text{reg}}^{\text{tot}} = \gamma_{\text{reg}} \left[1 + \frac{n_{\text{reg}} + \sqrt{n_{\text{reg}}^2 - n_{\text{reg}} + \kappa}}{\kappa - n_{\text{reg}}} \right]. \quad (35)$$

and fit this prediction to the experimental data, that is number of detected high- Q modes, and their linewidths. Figure 12 shows that Eq. (35) does qualitatively capture the behavior of the average linewidths of the regular modes, within some errors. The fitted value for γ_{reg} corresponds to an average intrinsic Q factor of the order of $10^6 - 10^7$, which is consistent with the values measured in an independent experiment, where the regular modes are excited directly via fiber-taper coupling (Appendix B), and there is virtually no coupling to the chaotic modes (Fig. 13). Thus, the systematic enlargement of the average linewidths with the number of observed regular modes supports the approximations leading to Eq. (33).

VI. CONCLUSION AND DISCUSSION

We count statistics of chaotic resonances in a deformed optical microcavity by the sole experimental detection

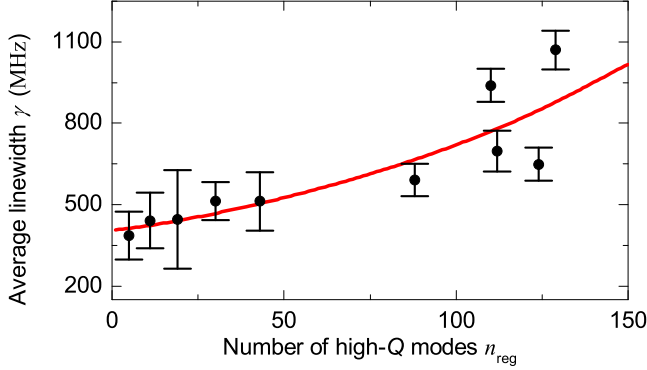


FIG. 12. Dots: average linewidth of the excited regular modes vs. their number. Each data point represents one experiment with a different size of the silicon pillar (here $\eta = 6\%$, $\lambda = 635$ nm). Line: Eq. (35), with $\gamma_{\text{reg}} = 385$ MHz, and $\kappa = 331$.

of high- Q regular modes, using the coupling between regular and chaotic modes, which occurs via dynamical tunneling.

Being a priori unaware of the typical escape time of the chaotic modes that effectively contribute to the excitation of the regular modes, we use the experimental data to validate: *i*) an entirely classical model, *ii*) a RMT-based, purely statistical prediction, which is independent from system-specific properties, and, finally, *iii*) a semiclassical correction to *ii*), which does depend on the Lyapunov exponent of the chaotic dynamics, and that is found in the best agreement with the observations.

The estimation of the Ehrenfest time of quantum-to-classical correspondence from the experimental parameters plays a key role in framing the time scale of the decay (or typical linewidth) of the chaotic states (resonances). The fastest escape occurs around Ehrenfest time, and generally within the average time of transition of the decay of correlations from exponential to algebraic, so that the classical description of the dynamics as fully chaotic seems appropriate.

On the other hand, accounting for the long-lived chaotic resonances does not seem to be as straightforward. Specifically, the effects of partial transport barriers, as well as the ‘stickiness’ along KAM tori and stability islands are relegated to the fitting parameters in the current model. The correct detection and modelling of long-lived resonances are therefore primary issues to be addressed by future work, especially in perspective of a test of fractal Weyl law at optical frequencies. Other challenges include the possibility of estimating and measuring the amplitude of the regular-to-chaotic mode coupling, as well as developing a more refined prediction for the excitation of the regular modes.

VII. ACKNOWLEDGMENTS

This project was supported by the 973 program (Grant Nos. 2013CB921904 and 2013CB328704), the NSFC (Grant Nos. 61435001 and 11474011). DL acknowledges support from NSFC (Grant No. 11450110057-041323001).

Appendix A: Rescaling the Lyapunov exponent

The classical estimate of the prefactor $MN^{-1/\hat{\mu}\tau_d}$ involves Ehrenfest time, defined for *open* systems as [42]

$$\tau_{Ehr} = \frac{1}{\mu} \log \frac{\tau_H}{\tau_d}. \quad (\text{A1})$$

Here μ is the Lyapunov exponent of the closed system, τ_d is the mean dwell time, while τ_H is the Heisenberg time

$$\tau_H = \frac{h}{\Delta E}, \quad (\text{A2})$$

with ΔE mean level spacing, that is average distance (or difference) between consecutive energy levels. We know, on the other hand, that $E = h\nu$, and we may therefore express Heisenberg time in terms of the frequency spacing

$$\tau_H = \frac{1}{\Delta\nu}, \quad (\text{A3})$$

and Ehrenfest time as

$$\tau_{Ehr} = \frac{1}{\mu} \log \frac{N}{\Delta\Upsilon}. \quad (\text{A4})$$

Here N is the number of open channels as we know, whereas $\Delta\Upsilon = MT\Delta\nu$, that is the mean frequency spacing times the Poincaré time (to make it dimensionless), times the number of states M . In plain words, $\Delta\Upsilon$ is the frequency range of our modes in units of the Poincaré time. At this point we can still write

$$\tau_{Ehr} = \frac{1}{\hat{\mu}} \log N, \quad (\text{A5})$$

provided that

$$\hat{\mu} = \frac{\log N}{\log N - \log \Delta\Upsilon} \mu. \quad (\text{A6})$$

Thus we have determined the rescaling to the Lyapunov exponent, following the definition of the Ehrenfest time.

Appendix B: Fiber-taper coupling

In Fig. 13(a) we provide an independent cross-check that many high- Q modes ($Q > 10^5$) do exist in the deformed microcavity, by exciting them directly through a tapered fiber [58]. Here the silicon pillar attached to the

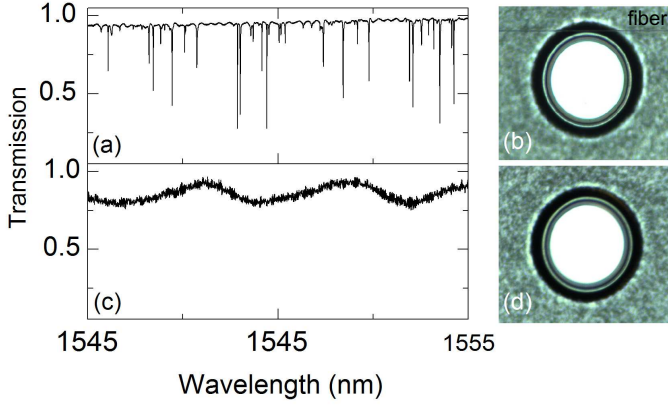


FIG. 13. Normalized transmission and top-view images of the cavity coupled by fiber taper [(a) and (b)], notice the fiber beside the cavity and free-space laser beam [(c) and (d)]. The resonances in (a) have Q factors typically of the order of $10^6 - 10^7$. Here the absorber-to-cavity ratio is $r \simeq 0.83$.

microtoroid has largest size, so that dynamical tunneling is inhibited and no whispering-gallery mode can be excited with the free-space coupling [Fig. 13(c)]. By reducing the size of the silicon pillar, as shown in Fig. 8, high- Q modes can be excited indirectly by a free-space beam.

Appendix C: Estimation of Ehrenfest time

Let us start from the definition of the Ehrenfest time

$$\tau_{Ehr} = \frac{1}{\mu} \ln \frac{\tau_H}{\tau_d}, \quad (C1)$$

with

$$\tau_H = \frac{h}{\Delta E} = \frac{1}{\Delta\nu}, \quad (C2)$$

$$\tau_d = \frac{M}{N} T, \quad (C3)$$

and T is the Poincaré time. For visible light, we observe about 100 WGMs in a range of wavelengths of about 10nm, hence an estimated mean spacing between consecutive regular modes $\Delta\lambda \sim 10^{-10}$. Then

$$\Delta\nu \simeq \frac{c\Delta\lambda}{\lambda^2} \sim \frac{2 \cdot 10^8 \cdot 10^{-10}}{6^2 \cdot 10^{-14}} = 5 \cdot 10^{10} \text{Hz}, \quad (C4)$$

while

$$T \simeq \frac{a}{2c} \sim \frac{6 \cdot 10^5}{2 \cdot 10^8} = 3 \cdot 10^{-13} \text{s}, \quad (C5)$$

with a principal diameter of the microcavity. That way,

$$\tau_{Ehr} = \frac{1}{\mu} \ln \frac{\xi}{\Delta\nu AT}, \quad (C6)$$

where we took $\xi \simeq \frac{A}{\tau_d}$ (neglecting refraction into air), and $A = 2\pi(\sin\theta_{max} - \sin\theta_{th})$, area of the phase space available to chaotic states above $\sin\theta_{th}$.

-
- [1] S. L. McCall, A. F. J. Levi, R. E. Slusher, S. J. Pearton, and R. A. Logan, Whispering-gallery mode microdisk lasers, *Appl. Phys. Lett.* **60**, 289-291 (1992).
 - [2] K. J. Vahala, Optical microcavities, *Nature* **424**, 839-846 (2003).
 - [3] A. B. Matsko and V. S. Ilchenko, Optical resonators with whispering gallery modes I: basics, *IEEE J. Sel. Top. Quantum Electron* **12**, 3 (2006).
 - [4] H. Cao and J. Wiersig, Dielectric microcavities: Model systems for wave chaos and non-Hermitian physics, *Rev. Mod. Phys.* **87**, 61 (2015).
 - [5] L. Shao, X.-F. Jiang, X.-C. Yu, B.-B. Li, W. R. Clements, F. Vollmer, W. Wang, Y.-F. Xiao, and Q. Gong, Detection of single nanoparticles and lentiviruses using microcavity resonance broadening, *Adv. Mater.* **25**, 5616-5620 (2013).
 - [6] Y.-S. Park and H. Wang, Resolved-sideband and cryogenic cooling of an optomechanical resonator, *Nature Phys.* **5**, 489-493 (2009).
 - [7] J. U. Nöckel and A. D. Stone, Ray and wave chaos in asymmetric resonant optical cavities, *Nature* **385**, 45 (1997).
 - [8] C. Gmachl, F. Capasso, E. E. Narimanov, J. U. Nöckel, A. D. Stone, J. Faist, D. L. Sivco, and A. Y. Cho, High-power directional emission from microlasers with chaotic resonators, *Science* **280**, 1556-1564 (1998).
 - [9] J. Wiersig and M. Hentschel, Combining directional light output and ultralow loss in deformed microdisks, *Phys. Rev. Lett.* **100**, 033901 (2008).
 - [10] S. Shinohara, T. Harayama, T. Fukushima, M. Hentschel, T. Sasaki, and E. E. Narimanov, Chaos-assisted directional light emission from microcavity lasers, *Phys. Rev. Lett.* **104**, 163902 (2010).
 - [11] Q. H. Song, L. Ge, A. D. Stone, H. Cao, J. Wiersig, J.-B. Shim, J. Unterhinninghofen, W. Fang, and G. S. Solomon, Directional laser emission from a wavelength-scale chaotic microcavity, *Phys. Rev. Lett.* **105**, 103902 (2010).
 - [12] Channeling chaotic rays into waveguides for efficient collection of microcavity emission, Q. H. Song, L. Ge, B. Redding, and H. Cao, *Phys. Rev. Lett.* **108**, 243902 (2012).
 - [13] X.-F. Jiang, Y.-F. Xiao, C.-L. Zou, L. He, C.-H. Dong, B.-B. Li, Y. Li, F.-W. Sun, L. Yang, and Q. Gong, Highly Unidirectional Emission and Ultralow-Threshold Lasing from On-Chip Ultrahigh-Q Microcavities, *Adv. Mater.* **24** OP260 (2012).
 - [14] J. Ward and O. Benson, WGM microresonators: sensing, lasing and fundamental optics with microspheres, *Laser*

- Photonics Rev. **5**, 553 (2011).
- [15] S. Sunada and T. Harayama, Design of resonant microcavities: application to optical gyroscopes, Opt. Express **15**, 16245-16254 (2007).
 - [16] J. Wiersig, Formation of long-lived, scarlike modes near avoided resonance crossings in optical microcavities, Phys. Rev. Lett. **97**, 253901 (2006).
 - [17] J. Anderasen, H. Cao, J. Wiersig, and A. E. Motter, Marginally unstable periodic orbits in semiclassical mushroom billiards, Phys. Rev. Lett. **103**, 154101 (2009).
 - [18] S. Shinohara, T. Harayama, T. Fukushima, M. Hentschel, S. Sunada, and E. E. Narimanov, Chaos-assisted emission from asymmetric resonant cavity microlasers, Phys. Rev. A **83**, 053837 (2011).
 - [19] J. Yang, S.-B. Lee, S. Moon, S.-Y. Lee, S. W. Kim, T. T. A. Dao, J.-H. Lee, and K. An, Pump-induced dynamical tunneling in a deformed microcavity laser, Phys. Rev. Lett. **104**, 243601 (2010).
 - [20] Y.-F. Xiao, X.-F. Jiang, Q.-F. Yang, L. Wang, K. Shi, Y. Li, Q. Gong, Tunneling-induced transparency in a chaotic microcavity, Laser Photonics Rev. **7**, L51 (2013).
 - [21] V. A. Podolskiy, E. Narimanov, W. Fang, and H. Cao, Chaotic microlasers based on dynamical localization, Proc. Natl. Acad. Sci. U.S.A. **101**, 10498-10500 (2004).
 - [22] W. Fang, H. Cao, V. A. Podolskiy, and E. E. Narimanov, Dynamical localization in microdisk lasers Opt. Express **13**, 5641-5652 (2005).
 - [23] S. B. Lee, J. H. Lee, J. S. Chang, H. J. Moon, S. W. Kim, and K. An, Observation of scarred modes in asymmetrically deformed microcylinder lasers, Phys. Rev. Lett. **88**, 033903 (2002).
 - [24] N. B. Rex, H. E. Tureci, H. G. L. Schwefel, R. K. Chang, and A. D. Stone, Fresnel filtering in lasing emission from scarred modes of wave-chaotic optical resonators, Phys. Rev. Lett. **88**, 094102 (2002).
 - [25] C. Gmachl, E. E. Narimanov, F. Capasso, J. N. Bailargeon, and A. Y. Cho, Kolmogorov-Arnold-Moser transition and laser action on scar modes in semiconductor diode lasers with deformed resonators, Opt. Lett. **27**, 824-826 (2002).
 - [26] J.-B. Shim, S.-B. Lee, S. W. Kim, S.-Y. Lee, J. Yang, and S. Moon, Uncertainty-limited turnstile transport in deformed microcavities, Phys. Rev. Lett. **100**, 174102 (2008).
 - [27] S. B. Lee, J. Yang, S. Moon, S.-Y. Lee, S. W. Kim, J.-H. Lee, and K. An, Quasieigenstate evolution in open chaotic billiards, Phys. Rev. A **80**, 011802 (2009).
 - [28] M. V. Berry and M. Robnik, Semiclassical level spacings when regular and chaotic orbits coexist, J. Phys. A **17**, 2413 (1984).
 - [29] P. Gaspard and S. A. Rice, Semiclassical quantization of the scattering from a classically chaotic repeller, J. Chem. Phys. **90**, 2242-2254 (1989).
 - [30] P. So, S. M. Anlage, E. Ott, and R. N. Oerter, Wave chaos experiments with and without time reversal symmetry: GUE and GOE statistics, Phys. Rev. Lett. **74**, 2662 (1995).
 - [31] E. N. Pozzo, D. Domínguez, and M. J. Sánchez, Quantum chaos in the mesoscopic device for the Josephson flux qubit, Phys. Rev. B **77**, 024518 (2008).
 - [32] J. Wiersig and J. Main, Fractal Weyl law for chaotic microcavities: Fresnel's laws imply multifractal scattering, Phys. Rev. E **77**, 036205 (2008).
 - [33] A. Potzuweit, T. Weich, S. Barkhofen, U. Kuhl, H.-J. Stöckmann, and M. Zworski, Weyl asymptotics: From closed to open systems, Phys. Rev. E **86**, 066205 (2012).
 - [34] S. Nonnenmacher and E. Schenck, Resonance distribution in open quantum chaotic systems, Phys. Rev. E **78**, 045202 (2008).
 - [35] M. Schönwetter and E. G. Altmann, Quantum signatures of classical multifractal measures, Phys. Rev. E **91**, 012919 (2015).
 - [36] E. G. Altmann, J. S. E. Portela, and T. Tél, Chaotic Systems with Absorption, Phys. Rev. Lett. **111**, 144101 (2013).
 - [37] L. Wang, D. Lippolis, Z. Y. Li, X. F. Jiang, Q. Gong, and Y. F. Xiao, Statistics of chaotic resonances in an optical microcavity, Phys. Rev. E **93**, 040201(R), 2016.
 - [38] K. Życzkowski and H. J. Sommers, Truncations of random unitary matrices, J. Phys. A **33**, 2045 (2000).
 - [39] H. Schomerus and J. Tworzydło, Quantum-to-classical crossover of quasibound states in open quantum systems, Phys. Rev. Lett. **93**, 154102 (2004).
 - [40] W. T. Lu, S. Sridhar, and M. Zworski, Fractal Weyl Laws for Chaotic Open Systems, Phys. Rev. Lett. **91**, 154101 (2003).
 - [41] S. Nonnenmacher and M. Zworski, Fractal Weyl laws in discrete models of chaotic scattering, J. Phys. A **38**, 10683 (2005).
 - [42] H. Schomerus and Ph. Jacquod, Quantum-to-classical correspondence in open chaotic systems, J. Phys. A **38**, 10663 (2005).
 - [43] M. J. Davis and E. J. Heller, Quantum dynamical tunneling in bound states, J. Chem. Phys. **75**, 246-254 (1981).
 - [44] K. An and J. Yang, Mode-mode coupling theory of resonant pumping via dynamical tunneling processes in a deformed microcavity, in *Trends in Nano- and Micro-Cavities* (Bentham Science, Sharjia, U.A.E, 2011) pp.40-61.
 - [45] K. An, Semiclassical theory of the many-atom microlaser, J. Korean Phys. Soc. **42**, 505 (2003).
 - [46] R. W. Boyd, *Nonlinear Optics* (Academic Press, Boston, 2009).
 - [47] U. Fano, Effects of configuration interaction on intensities and phase shifts, Phys. Rev. **124**, 1866 (1961).
 - [48] Q.-F. Yang, X.-F. Jiang, Y.-L. Cui, L. Shao, and Y.-F. Xiao, Dynamical tunneling-assisted coupling of high-Q deformed microcavities using a free-space beam, Phys. Rev. A **88**, 023810 (2013).
 - [49] Precisely, we suppose they are biorthogonal, given the non-Hermiticity of the Hamiltonian. See, for example, S.-Y. Lee, Decaying and growing eigenmodes in open quantum systems: Biorthogonality and the Petermann factor, Phys. Rev. A **80**, 042104 (2009).
 - [50] H. J. Stöckmann, "Quantum Chaos: an Introduction," Cambridge University Press, Cambridge (1999).
 - [51] M. J. Körber, M. Michler, A. Bäcker, and R. Ketzmerick, Hierarchical Fractal Weyl Laws for Chaotic Resonance States in Open Mixed Systems, Phys. Rev. Lett. **111**, 114102 (2013).
 - [52] A. Ishii, A. Akaishi, A. Shudo, and H. Schomerus, Weyl law for open systems with sharply divided mixed phase space, Phys. Rev. E **85**, 046203 (2012).
 - [53] J. Meiss, Symplectic maps, variational principles, and transport, Rev. Mod. Phys. **64**, 79 (1992).
 - [54] M. Michler, A. Bäcker, R. Ketzmerick, H.-J. Stöckmann, and S. Tomsovic, Universal quantum localizing transition

- of a partial barrier in a chaotic sea, Phys. Rev. Lett. **109**, 234101, (2012).
- [55] Y. C. Lai, and T. Tél, *Transient Chaos* (Springer, New York, 2010).
- [56] J. R. Taylor, *An Introduction to Error Analysis* (University Science Books, Sausalito, CA, 1997).
- [57] Ph. Jacquod and E. V. Sukhorukov, Breakdown of Universality in Quantum Chaotic Transport: The Two-Phase Dynamical Fluid Model, Phys. Rev. Lett. **92**, 116801, (2004).
- [58] M. Cai, O. Painter, and K. J. Vahala, Observation of Critical Coupling in a Fiber Taper to a Silica-Microsphere Whispering-Gallery Mode System, Phys. Rev. Lett. **85**, 74 (2000).